JACS
JOURNAL OF THE AMERICAN CHEMICAL SOCIETY
Article
pubs.acs.org/JACS

Real-Space Imaging of the Atomic Structure of Organic–Inorganic Perovskite

Robin Ohmann,[†] Luis K. Ono,[†] Hui-Seon Kim,[‡] Haiping Lin,[§] Michael V. Lee,[†,⊥] Youyong Li,[*,§] Nam-Gyu Park,[*,‡] and Yabing Qi[*,†]

[†]Energy Materials and Surface Sciences Unit (EMSS), Okinawa Institute of Science and Technology Graduate University (OIST), 1919-1 Tancha, Onna-son, Okinawa 904-0495, Japan

[‡]School of Chemical Engineering and Department of Energy Science, Sungkyunkwan University (SKKU), Suwon 440-746, Korea

[§]Institute of Functional Nano and Soft Materials (FUNSOM), Soochow University, Suzhou 215123, P. R. China

Supporting Information

ABSTRACT: Organic–inorganic perovskite is a promising class of materials for photovoltaic applications and light emitting diodes. However, so far commercialization is still impeded by several drawbacks. Atomic-scale effects have been suggested to be possible causes, but an unequivocal experimental view at the atomic level is missing. Here, we present a low-temperature scanning tunneling microscopy study of single crystal methylammonium lead bromide $CH_3NH_3PbBr_3$. Topographic images of the in situ cleaved perovskite surface reveal the real-space atomic structure. Compared to the bulk we observe modified arrangements of atoms and molecules on the surface. With the support of density functional theory we explain these by surface reconstruction and a substantial interplay of the orientation of the polar organic cations $(CH_3NH_3)^+$ with the position of the hosting anions. This leads to structurally and electronically distinct domains with ferroelectric and antiferroelectric character. We further demonstrate local probing of defects, which may also impact device performance.

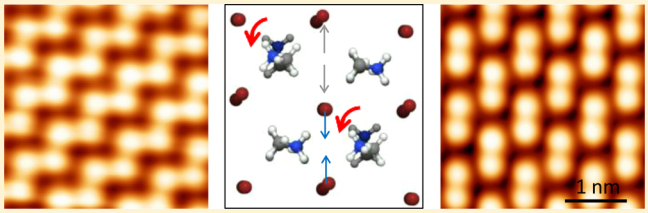

INTRODUCTION

Organometal halide perovskites are currently one of the most actively researched materials. They are typically composed of an organic group (A), a metal ion (B), and one or two halides (X) forming the perovskite structure ABX_3. In particular, the methylammonium lead halide perovskites, namely, $CH_3NH_3PbX_3$ (X = Br, I, Cl), show remarkable properties for photovoltaic applications[1−4] and light emitting diodes.[5] Solar power conversion efficiencies of more than 20% have been reported,[6] and widely tunable light emitting diodes have been realized.[7] Their low cost and ease of production make them suitable candidates for future technologies. Current challenges that impede the commercialization of the perovskite include rapid device degradation,[8,9] hysteresis,[10,11] and sensitivity to environmental factors such as humidity and temperature.[12] Additionally, atomic-scale defects can strongly influence the behavior of the solar cell absorber.[13−15] Prototype devices are typically made as sandwiches of several thin films.[11] In particular, not only the bulk properties but also the interfaces between films are of paramount importance for device performance. Analytical methods employed for characterization have not been able to resolve the atomic structure of the first layer.[16] Hence, an atomic-scale picture of the perovskite surface has not been achieved so far. Furthermore, there is an ongoing debate about the effects of the methylammonium (MA) ions. Their orientation is theoretically predicted to play a decisive role in the structural and electronic properties of the perovskite.[17,18] This is attributed to their dipole character, which is fundamentally different from the spherical symmetry of the cations in purely inorganic perovskites. Although there has been recent experimental progress,[19] the exact orientation of the dipoles within the lattice and especially the interplay of the methylammonium groups with the hosting anions have not been reported so far.

To obtain a detailed view of the atomic-scale morphology and electronic properties of a conducting surface the scanning tunneling microscope (STM) is a suitable tool. It has been used successfully to characterize inorganic perovskites such as oxides[20] and manganites.[21,22] However, to the best of our knowledge, no report shows imaging on any organometal halide perovskite. In part, this may be due to the challenge of obtaining a clean atomically flat surface. The production of thin perovskite films is typically achieved via solution process methods.[23] However, these processes involve exposure to air or solvents, and thus, the surfaces are expected to be contaminated with adsorbates and are polycrystalline. A better defined surface is required for STM investigations.

Here, we present a scanning tunneling microscopy study on an in situ cleaved single crystal organometal halide perovskite.

Received: August 5, 2015
Published: December 6, 2015

DOI: 10.1021/jacs.5b08227
J. Am. Chem. Soc. 2015, 137, 16049−16054

$CH_3NH_3PbBr_3$ was chosen because large single crystals can easily be grown and, like its sister lead triiodide perovskite, this material also has exceptional photovoltaic properties,[24] with even better stability in air, and is a promising candidate for light emitting diodes.[5] The crystal was cleaved under ultrahigh vacuum conditions to ensure a clean flat surface free of contaminants. Our experimental results are corroborated by density functional theory (DFT) calculations allowing assignment of the imaged atoms and the structure. To match the experimental images, a surface reconstruction and specific orientations of the methylammonium organic groups $(CH_3NH_3)^+$ are revealed, demonstrating that the MA groups align in certain patterns resulting in discrete domains.

RESULTS AND DISCUSSION

Methylammonium lead bromide ($CH_3NH_3PbBr_3$) single crystals were grown in solution (see Methods section for details). Crystals were cleaved in situ with a scalpel and subsequently transferred into the custom-built low-temperature scanning tunneling microscope (STM) held at T = 4.5 K and operated under ultrahigh vacuum conditions (base pressure below 10^{-10} mbar).

An STM topography image with atomic resolution of the $CH_3NH_3PbBr_3$ surface is shown in Figure 1a. Bright protrusions with a corrugation of a few tenths of an angstrom are observed. The protrusions are arranged in an alternating fashion with short and long distances between the next neighbor in both horizontal and vertical direction (see inset). As will be shown below, they can be assigned to the Br atoms. In Figure 1b a step edge of the crystal is imaged. Upper and lower terraces reveal the same atomic arrangement, evidencing that they belong to the same surface layer. The step-height averaged over several images is 5.3 ± 0.4 Å. In order to understand which layers and which atoms are imaged, DFT calculations were performed. Since these measurements were carried out at a temperature of T = 4.5 K, the crystal is expected to possess the orthorhombic phase, which exists below the phase transition temperature of T = 144.5 K.[25] The unit cell was calculated to be 7.87 Å × 12.02 Å × 8.79 Å, which is in very good agreement (less than 3% deviation) with experiments.[26] Using the bulk values for the surface did not match the experimental STM observations. Also, the surface is not stable when the bulk lattice parameters are assumed. The energy minimum is found only when surface reconstruction takes place. A calculated STM image of the reconstructed surface is shown in Figure 1c agreeing very well with the experimental results. The bright protrusions in the STM image can thus be assigned to the Br atoms, and the crystallographic plane is the (010) surface of the orthorhombic crystal. The assignment of the plane follows the nomenclature presented in ref 16. The MA molecules are oriented perpendicular to each other (see Figure 1c) with an overall nonzero surface dipole resembling a ferroelectric. In Figure 1d the difference between the bulk terminated and reconstructed surface is shown. The positions of the top layer atoms shift by about 10% for the reconstruction. Strikingly, the long axis of the methylammonium group is no longer parallel with the surface plane, but rotated by 40° such that the N atom is about 0.7 Å below the surface spanned by the C and Br atoms, which are at about the same height. Additionally, minor atom shifts occur in the second layer, which is composed only of Pb and Br atoms. The energy gain for the reconstructed surface is calculated to be approximately 0.50 eV per unit cell.

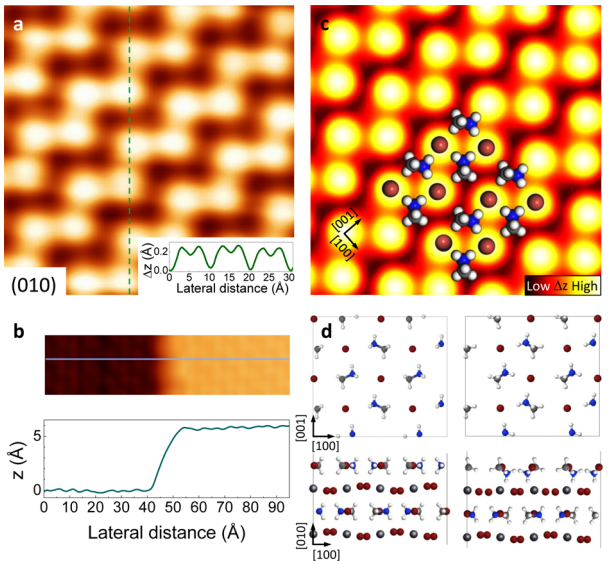

Figure 1. Atomic resolution of $CH_3NH_3PbBr_3$. (a) Atomically resolved STM topography image of the perovskite surface. Inset: Height profile along dashed line in the image. Image size: 31 × 31 Å^2. Scan parameters: Bias = −5 V and I = 0.1 nA. (b) STM image of a step edge. Bottom: Height profile. (c) Simulated STM image of the (010) plane of the orthorhombic crystal with surface reconstruction. Br and MA ions are overlaid. (d) (Left panels) Top and side view of the unreconstructed surface. (Right panels) Top and side view of the reconstructed surface. Color code: N (blue), C (gray), H (white), Br (brown), Pb (black with white highlight).

These results indicate that the surface MA groups are free to rotate out-of plane. Additionally, they are also free to rotate in-plane, which will be shown as follows. Besides the atomic structure displayed in Figure 1, other coexisting structures were observed. The dominant one is shown in Figure 2a. The structural difference can be clearly seen when taking height profiles along two perpendicular directions (see Figure 2c). For one direction an alternating arrangement of short and long distances, similar to the first structure, is observed. However, in the perpendicular direction the atoms are equally spaced, which is in contrast to the first structure. To explain this structure we calculated the surface with different in-plane orientations of MA. The best match was achieved for an antiferroelectric alignment of the MA groups as shown in Figure 2b. Each MA group is aligned in an alternating fashion. This also causes the Br atoms to relax, explaining the different structure. The interaction between polar MA groups and negatively charged Br ions is of electrostatic nature.[27] As can be seen in Figure 2b, short Br−Br distances are observed, when the positive side of the dipole (the N atom) is nearby. The attractive interaction shortens the Br−N distance drawing the pairs of Br ions closer together. In contrast, Br ions are repelled by the negative side of the dipole (the C atom) leading to a much larger separation of Br atoms. This is evident for both structures. Importantly, each Br−Br pair has two MA neighbors, which show depending on the structure different orientations with respect to each other. For example, the smallest Br−Br distance is observed when both MAs have their N-terminated sides toward the bromine pair. In general, the Br−Br bond length increases for a lesser contribution of N and an increased contribution of C in the following order of neighboring MA combinations: Br−$Br_{(N,N)}$ (3.7 ± 0.1 Å), Br−$Br_{(N,parallel)}$ (4.6 ± 0.3 Å), Br−$Br_{(parallel,antiparallel)}$ (5.1 ± 0.3 Å), Br−$Br_{(C,parallel)}$ (5.8 ± 0.3 Å),

DOI: 10.1021/jacs.5b08227
J. Am. Chem. Soc. 2015, 137, 16049−16054

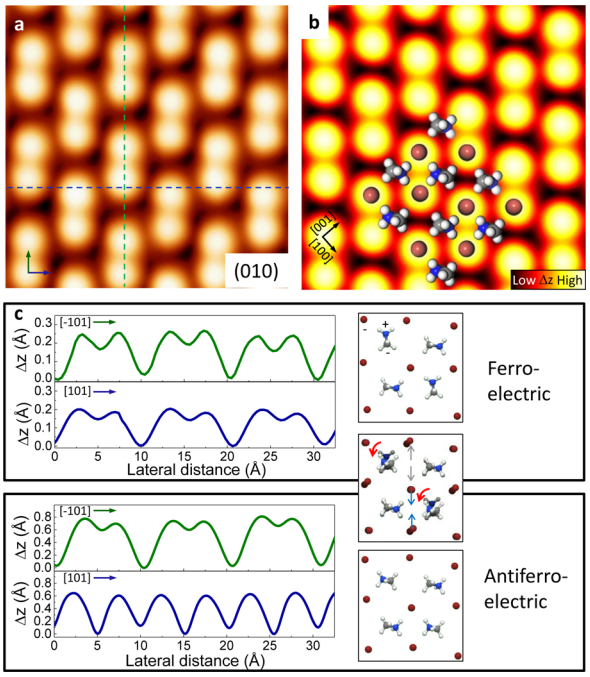

Figure 2. Orientation of MA leading to different domains. (a) STM topography image of another domain than that shown in Figure 1. Image size: 31 × 31 Å^2. Bias = −9 V, and I = 0.1 nA. The arrows and dashed lines indicate the direction of the height profiles shown in part c, bottom. (b) Corresponding calculated image. (c) Comparison of height profiles along perpendicular directions for two different observed domains ((top) Figure 1 and (bottom) Figure 2) and the corresponding model. The arrows indicate the rotational and positional change of the MA molecules and the Br ions, respectively, between the ferroelectric and antiferroelectric domain. For better comparison the ferroelectric representation is reduced in brightness in the central image.

Br−Br$_{(C,C)}$ (6.6 ± 0.2 Å), where parallel refers to an MA which is oriented parallel to the Br−Br pair and N and C refer to MA which is facing either with the N- or C-terminated side towards the Br−Br pair. This shows the strong interplay of the MA with the Br ions and emphasizes the importance of the polar molecule as a cation present in organic−inorganic perovskite. We note that the antiferroelectric structure is 0.51 eV per unit cell lower in energy than the ferroelectric structure, which is consistent with the experimental observation of a larger area covered by antiferroelectric domains compared to ferroelectric ones. During the cooling process the surface is quenched into the different domains.

Methylammonium groups can be visualized at defined scanning conditions. When the tip is brought closer to the surface, by increasing the current or decreasing the voltage, the methylammonium group can be imaged. In Figure 3a the surface is imaged at −5 V, and in Figure 3b the same area is imaged at −3 V. In the latter, additional protrusions appear, which are assigned to methylammonium. In Figure 3c, a simulated STM image calculated for a shorter tip−sample distance shows additional protrusions at the positions of the methylammonium groups. The need for a closer distance is related to the shorter extent of the density of states into the vacuum of the MA compared to the Br atoms as shown in Figure 3e. Interestingly, the MA is imaged, despite having two main atoms, only as one protrusion. This is attributed to the out-of plane orientation, resulting in one atom being closer to the surface than the other and the different local density of states for the carbon and nitrogen atom of the MA. Even though the MA molecules in the surface layer are the same, the protrusions have different intensities appearing in an alternating fashion as brighter and darker ones. This difference is ascribed to the distinct position and orientation of subsurface layer atoms and molecules, which influence the top layer.[28]

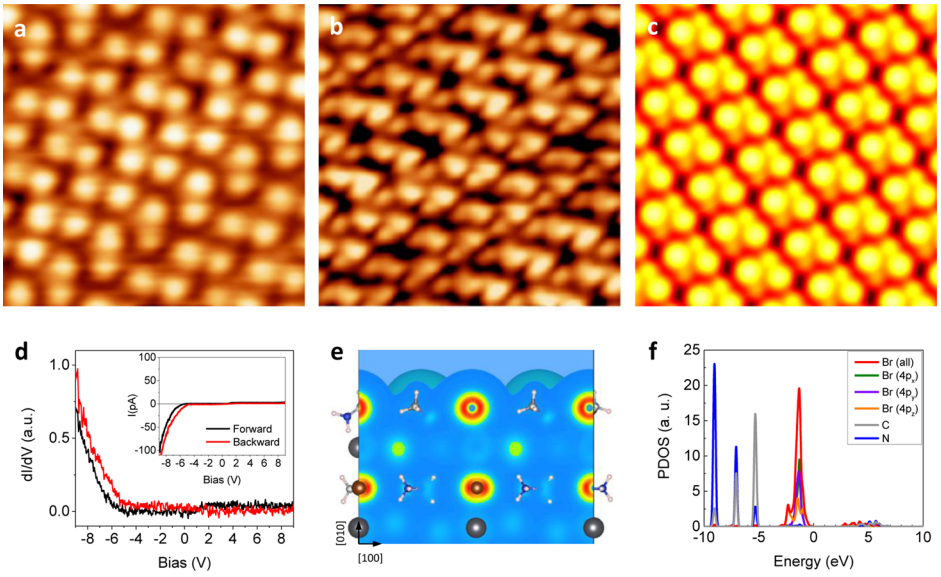

Figure 3. Visualization of MA and the electronic structure of $CH_3NH_3PbBr_3$. (a and b) Atomically resolved STM topography images of perovskite $CH_3NH_3PbBr_3$. Both images were taken at the same area, but under different scanning conditions. (a) Bias = −5 V. (b) Bias = −3 V. Current: 0.1 nA. Image size: 42 × 42 Å^2. (c) Calculated STM image with a small tip−sample distance. The MA molecules are additionally visualized. (d) Scanning tunneling spectroscopy (dI/dV) on the perovskite surface. Inset: Simultaneously acquired $I(V)$-curve. (e) Side view of the orbitals. (f) Calculated partial density of states (PDOS) of the surface in the antiferroelectric configuration. The indices 4p$_x$, 4p$_y$, and 4p$_z$ denote the specific contribution of each orbital.

DOI: 10.1021/jacs.5b08227
J. Am. Chem. Soc. 2015, 137, 16049−16054

To study the electronic properties, we acquired scanning tunneling spectra by keeping the tip stabilized at a fixed position above the surface while ramping the voltage (see Methods section). A typical spectrum is displayed in Figure 3d. Only for negative voltages, which reveal the occupied states of the surface, we found an appreciable differential conductance (dI/dV). This is consistent with the difficulty (impossibility) in obtaining topographic images at positive voltages, i.e., unoccupied states, where no appreciable tunneling current was measurable, which is necessary for imaging. Calculated partial density of states support this observation (see Figure 3f). Only for the occupied states is a significant density of states obtained. Tunneling occurs predominantly in the protruding $4p_z$-states of Br and the carbon and nitrogen states of MA, provided that the tip is close enough. A comparison of the local density of states of the ferro- and antiferroelectric domain is presented in the Supporting Information revealing that the two morphologies lead to different electronic structures. These might influence the light-harvesting properties of perovskite locally and modify coupling to the adjacent interfaces in the layered device architecture. We note that the electronic properties observed at low-temperature are different than those at room-temperature. At room-temperature the crystal stabilizes in the cubic phase.[25] A typical spectrum obtained at room-temperature is shown in the Supporting Information. Initial experiments with light exposure onto the perovskite crystal reveal a strong increase of the tunneling current, indicating the creation of additional free charge carriers and tunneling channels. Piezoresponse force microscopy measurements by Kim et al.[29] show that light and bias induced polarization on $CH_3NH_3PbI_3$ can also be beneficial to the charge transport by providing effective electronic pathways.

Finally, we discuss the observation of dislocations and defects. In Figure 4a the onset of two dislocations is present (see arrow markers). Two Br atoms, which are close together are now oriented perpendicularly with respect to the main Br pair alignment. This rotation progresses in a diagonal fashion (45° with respect to the main axis) throughout the surface. The immediate neighboring pairs are also affected and are oriented slightly off-line (see white lines in Figure 4a) resulting in local ion arrangements displaying a chiral pattern. The dislocation lines are observed as a single or multiples (see inset of Figure 4a) or may occur in a periodic arrangement (see bottom panel of Figure 4a). Comparing image a and b of Figure 3, where dislocation lines appearing also as perpendicular Br pairs are visualized, one can see that the Br atoms have the same apparent height, but the MA molecules change contrast at the dislocation line. The contrast change is ascribed to a modified orientation of the MA, which in turn influences the position of the Br host anions. Our results reveal thus an additional role of the interplay of MA with Br ions very locally changing the structure of the perovskite.

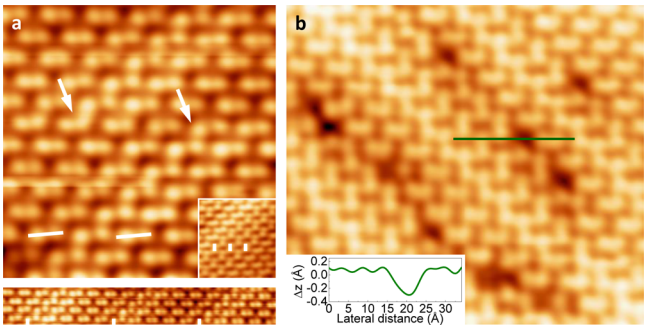

Figure 4. Dislocations and defects visualized with STM. (a) Start of dislocation rows indicated by white arrow. The angled lines indicate the modified Br atom positions adjacent to a dislocation row. Inset: Three dislocation rows beside each other. Bottom: Periodic arrangement of dislocation rows. The small white rectangles are guides to the eye indicating positions of dislocation rows. (b) STM image of defects on the surface. Inset: Height profile across a defect along green line indicated in the image. Image sizes: (a) 64 × 64 Å^2, inset 56 × 55 Å^2, bottom 164 × 23 Å^2; (b) 92 × 103 Å^2. Bias = −9 V. Current = 0.1 nA.

The role of defects on the device performance is a highly important topic in view of recent results on doping and self-doping,[13,14,30] defect migration,[15] and molecular vapor additives[31,32] potentially modifying the electronic structure of the material. Defects have been predicted to cause, depending on the type of defect, p-type or n-type behavior, thus influencing directly the conductivity of the material.[13,14] Also, defects play an important role in the degradation behavior as shown by ref 15, which discusses defect migration. Although atomic defects on organic−inorganic perovskite have been theoretically discussed and their influence on the material properties has been estimated, so far very few experimental studies have been reported to probe them. Here, we show for the first time the real-space observation of the defects in organic−inorganic perovskite. While for most of the images we have acquired the surface was rather defect-free (we were able to observe areas of >100 nm^2 with no defects; see overview and large area STM images in the Supporting Information), in Figure 4b an area with a particular high concentration of defects is presented. Here, about 10 defects per 100 nm^2 are visualized. On average the density of impurities is well below 1% with respect to the number of Br surface atoms, corresponding to fewer than three defects per 100 nm^2. All defects shown in the image appear as depressions, the most predominant type observed on the surface. We tentatively assign these defects to Br vacancies. We note, however, to find a clear proof for the type of defects observed, atomic force microscopy experiments[33,34] allowing chemical contrast will be useful.

CONCLUSION

In conclusion, we have shown atomic resolution topography images of in situ cleaved single crystal $CH_3NH_3PbBr_3$ perovskite. On the basis of density functional theory we were able to assign the observed protrusions to Br atoms of the reconstructed (010) plane of the orthorhombic crystal. Different surface structures were related to specifically aligned MA groups revealing their strong interplay with the Br anion host. Specifically, a ferroelectric and an antiferroelectric domain were identified. Furthermore, the MA was also imaged, for short tip−sample distances, appearing as an additional protrusion. The electronic structure reveals the contribution of Br orbitals and MA orbitals to the electron density on the surface and varies with the domain structure. Finally, we presented a detailed look at dislocation lines and defects. Our results are important for the understanding of the perovskite surface on the atomic scale. In particular, we showed the important role of the orientation of the organic group MA on the structure. Organic groups with different dipole strength would be worth exploring, and future research on adsorbed atoms and molecules, such as water molecules or dopants, will be of great interest, to determine on the atomic level their role in the electronic structure of the perovskite.

DOI: 10.1021/jacs.5b08227
J. Am. Chem. Soc. 2015, 137, 16049−16054

METHODS

Experiments. Methylammonium lead bromide $CH_3NH_3PbBr_3$ crystals were grown in solution using the procedure below following ref 35: $PbBr_2$ powder (0.37 g), CH_3NH_3Br powder (0.12 g), and dimethylformamide (DMF) (1 mL) were mixed in a glass vial until all material dissolved. The open vial was inserted in a glass beaker with larger diameter holding isopropanol alcohol (IPA) up to about half the height of the vial when inside the beaker. The beaker was then closed and sealed with plastic paraffin film and kept at room-temperature (T= 22 °C). After a few days crystals larger than 1 mm up to a maximum size of 7 mm were obtained. The crystal was mounted on a home-built sample holder and inserted into the ultrahigh vacuum system. Cleaving of the crystal was performed in situ with a scalpel, which was mounted on a linear-rotary-motion feedthrough. The cutting plane was parallel to one of the facets of the crystal, and the remaining thickness of the perovskite after cleavage was about 1−2 mm. Mechanical cleaving is not expected to induce atomic-scale defects, as evidenced in ref 36 for a structurally similar crystal, but possible surface modifications deviating from the bulk cannot be completely excluded.[37] A sketch of the sample holder and the contacts with the perovskite is shown in the Supporting Information to illustrate the sample geometry and the electrical contacts. After cleavage the sample was transferred into the low-temperature scanning tunneling microscope (base pressure $<1.0 \times 10^{-10}$ mbar), where it was cooled to T = 4.5 K. The use of low-temperatures allows study of the samples under well-controlled conditions, reducing mechanical drift of the setup and minimizing diffusion and dynamics of the material under investigation. Bias voltage refers to the sample voltage with respect to the tip. With application of a negative bias voltage, electrons are tunneling from the sample to the tip, and for a positive bias voltage electrons are tunneling from the tip to the sample. Simultaneously to the $I(V)$ curves the differential conductance $dI/dV(V)$ was measured with a lock-in amplifier set at a modulation voltage of 40 mV, a modulation frequency of 1024 Hz, and a time constant of 30 ms.

Theory. Density functional theory (DFT) calculations were performed with the VASP code.[38−41] The projector augmented wave (PAW) method with a kinetic energy of 400 eV was employed to describe electron−ion interactions. The generalized gradient approximation (GGA) with the Perdew−Burke−Ernzerhof (PBE) exchange-correlation functional was adopted to calculate exchange and correlation energy. For the unit cell, Brillouin zone (BZ) sampling was done using a 3 × 3 × 1 Monkhorst−Pack grid for all calculations. The $CH_3NH_3PbBr_3$ (010) surface was represented using a periodic slab based on the space group *Pnma*[26] containing seven atomic layers and a vacuum thickness of 25 Å. The bottom four layers of atoms were kept fixed, while the other atoms were allowed to relax. All structures were fully relaxed until the force on each atom was less than 0.01 eV per angstrom. Nonlocal effects were described with the vdw-DF functional of Langreth and Lundqvist.[42,43] From the electronic ground-state structure, STM images were calculated with the Tersoff−Hamann method implemented in the bSKAN code.[44−46]

ASSOCIATED CONTENT

Supporting Information

The Supporting Information is available free of charge on the ACS Publications website at DOI: 10.1021/jacs.5b08227.

Calculations of the partial density of states of the ferroelectric and antiferroelectric structure, additional scanning tunneling microscopy and spectroscopy data, and an illustration of the cleaving mechanism and the sample holder geometry (PDF)

AUTHOR INFORMATION

Corresponding Authors

*Yabing.Qi@OIST.jp
*npark@skku.edu
*yyli@suda.edu.cn

Present Address

[⊥]Department of Chemistry and Biochemistry, Northern Arizona University, 700 South Osborne Dr., Flagstaff, Arizona 86011-5698, United States

Notes

The authors declare no competing financial interest.

ACKNOWLEDGMENTS

R.O., L.K.O., M.V.L. and Y.B.Q. acknowledge funding from the Energy Materials and Surface Sciences Unit of the Okinawa Institute of Science and Technology Graduate University. Y.L. and H.L. acknowledge the National Natural Science Foundation of China (Grants 91233115 and 21273158). H.-S.K. and N.-G.P. acknowledge funding from the National Research Foundation of Korea (NRF-2012M3A6A7054861 (Global Frontier R&D Program on Center for Multiscale Energy System)). We thank S. Kirmayer and W. Ohmann for fruitful discussions on crystal growth.

REFERENCES

(1) Kojima, A.; Teshima, K.; Shirai, Y.; Miyasaka, T. *J. Am. Chem. Soc.* **2009**, *131*, 6050.
(2) Etgar, L.; Gao, P.; Xue, Z.; Peng, Q.; Chandiran, A. K.; Liu, B.; Nazeeruddin, M. K.; Grätzel, M. *J. Am. Chem. Soc.* **2012**, *134*, 17396.
(3) Lee, M. M.; Teuscher, J.; Miyasaka, T.; Murakami, T. N.; Snaith, H. J. *Science* **2012**, *338*, 643.
(4) Kim, H.-S.; Lee, C.-R.; Im, J.-H.; Lee, K.-B.; Moehl, T.; Marchioro, A.; Moon, S.-J.; Humphry-Baker, R.; Yum, J.-H.; Moser, J. E.; Grätzel, M.; Park, N.-G. *Sci. Rep.* **2012**, *2*, 591.
(5) Schmidt, L. C.; Pertegás, A.; González-Carrero, S.; Malinkiewicz, O.; Agouram, S.; Espallargas, G. M.; Bolink, H. J.; Galian, R. E.; Pérez-Prieto, J. *J. Am. Chem. Soc.* **2014**, *136*, 850.
(6) Yang, S. Y.; Noh, J. H.; Jeon, N. J.; Kim, Y. C.; Ryu, S.; Seo, J.; Seok, S., II *Science* **2015**, *348*, 1234.
(7) Zhang, F.; Zhong, H.; Chen, C.; Wu, X.-G.; Hu, X.; Huang, H.; Han, J.; Zou, B.; Dong, Y. *ACS Nano* **2015**, *9*, 4533.
(8) Niu, G.; Guo, X.; Wang, L. *J. Mater. Chem. A* **2015**, *3*, 8970.
(9) Misra, R. K.; Aharon, S.; Li, B.; Mogilyansky, D.; Visoly-Fisher, I.; Etgar, L.; Katz, E. *J. Phys. Chem. Lett.* **2015**, *6*, 326.
(10) Snaith, H. J.; Abate, A.; Ball, J. M.; Eperon, G. E.; Leijtens, T.; Noel, N. K.; Stranks, S. D.; Tse-Wei Wang, J.; Wojciechowski, K.; Zhang, W. *J. Phys. Chem. Lett.* **2014**, *5*, 1511.
(11) Raga, S. R.; Jung, M.-C.; Lee, M. V.; Leyden, M. R.; Kato, Y.; Qi, Y. *Chem. Mater.* **2015**, *27*, 1597.
(12) Han, Y.; Meyer, S.; Dkhissi, Y.; Weber, K.; Pringle, J. M.; Bach, U.; Spiccia, L.; Cheng, Y.-B. *J. Mater. Chem. A* **2015**, *3*, 8139.
(13) Shi, T.; Yin, W.-J.; Hong, F.; Zhu, K.; Yan, Y. *Appl. Phys. Lett.* **2015**, *106*, 103902.
(14) Yin, W.-J.; Shi, T.; Yan, Y. *Appl. Phys. Lett.* **2014**, *104*, 063903.
(15) Azpiroz, J. M.; Mosconi, E.; Bisquert, J.; De Angelis, F. *Energy Environ. Sci.* **2015**, *8*, 2118.
(16) Baikie, T.; Fang, Y.; Kadro, J. M.; Schreyer, M.; Wei, F.; Mhaisalkar, S. G.; Grätzel, M.; White, T. J. *J. Mater. Chem. A* **2013**, *1*, 5628.
(17) Frost, J. M.; Butler, K. T.; Brivio, F.; Hendon, C. H.; van Schilfgaarde, M.; Walsh, A. *Nano Lett.* **2014**, *14*, 2584.
(18) Motta, C.; El-Mellouhi, F.; Kais, S.; Tabet, N.; Alharbi, F.; Sanvito, S. *Nat. Commun.* **2015**, *6*, 7026.
(19) Leguy, A. M. A.; Frost, J. M.; McMahon, A. P.; Sakai, V. G.; Kochelmann, W.; Law, C. H.; Li, X.; Foglia, F.; Walsh, A.; O'Regan, B. C.; Nelson, J.; Cabral, J. T.; Barnes, P. R. F. *Nat. Commun.* **2015**, *6*, 7124.
(20) Stöger, B.; Hieckel, M.; Mittendorfer, F.; Wang, Z.; Fobes, D.; Peng, J.; Mao, Z.; Schmid, M.; Redinger, J.; Diebold, U. *Phys. Rev. Lett.* **2014**, *113*, 116101.
(21) Renner, Ch.; Aeppli, G.; Kim, B.-G.; Soh, Y.-A.; Cheong, S.-W. *Nature* **2002**, *416*, 518.

DOI: 10.1021/jacs.5b08227
J. Am. Chem. Soc. 2015, 137, 16049−16054

(22) Rößler, S.; Padmanabhan, B.; Elizabeth, S.; Bhat, H. L.; Steglich, F.; Wirth, S. *Appl. Phys. Lett.* **2010**, *96*, 202512.
(23) Grätzel, M.; Janssen, R. A. J.; Mitzi, D. B.; Sargent, E. H. *Nature* **2012**, *488*, 304.
(24) Heo, J. H.; Song, D. H.; Im, S. H. *Adv. Mater.* **2014**, *26*, 8179.
(25) Poglitsch, A.; Weber, D. *J. Chem. Phys.* **1987**, *87*, 6373.
(26) Mashiyama, H.; Kawamura, Y.; Kubota, Y. *J. Korean Phys. Soc.* **2007**, *51*, 850.
(27) Stepanow, S.; Ohmann, R.; Leroy, F.; Lin, N.; Strunskus, T.; Wöll, C.; Kern, K. *ACS Nano* **2010**, *4*, 1813.
(28) Ohmann, R.; Levita, G.; Vitali, L.; De Vita, A.; Kern, K. *ACS Nano* **2011**, *5*, 1360.
(29) Kim, H.-S.; Kim, S.-K.; Kim, B.-J.; Shin, K.-S.; Gupta, M. K.; Jung, H. S.; Kim, S.-W.; Park, N.-G. J. *J. Phys. Chem. Lett.* **2015**, *6*, 1729.
(30) Kim, J.; Lee, S.-H.; Lee, J. H.; Hong, K.-H. *J. Phys. Chem. Lett.* **2014**, *5*, 1312.
(31) deQuilettes, D. W.; Vorpahl, S. M.; Stranks, S. D.; Nagaoka, H.; Eperon, G. E.; Ziffer, M. E.; Snaith, H. J.; Ginger, D. S. *Science* **2015**, *348*, 683.
(32) Zhou, Z.; Wang, Z.; Zhou, Y.; Pang, S.; Wang, D.; Xu, H.; Liu, Z.; Padture, N. P.; Cui, G. *Angew. Chem., Int. Ed.* **2015**, *54*, 9705.
(33) Sugimoto, Y.; Pou, P.; Abe, M.; Jelinek, P.; Pérez, R.; Morita, S.; Custance, O. *Nature* **2007**, *446*, 64.
(34) Custance, O.; Pérez, R.; Morita, S. *Nat. Nanotechnol.* **2009**, *4*, 803.
(35) Tidhar, Y.; Edri, E.; Weissman, H.; Zohar, D.; Hodes, G.; Cahen, D.; Rybtchinski, B.; Kirmayer, S. *J. Am. Chem. Soc.* **2014**, *136*, 13249.
(36) Stöger, B.; Hieckel, M.; Mittendorfer, F.; Wang, Z.; Schmid, M.; Parkinson, G. S.; Fobes, D.; Peng, J.; Ortmann, J. E.; Limbeck, A.; Mao, Z.; Redinger, J.; Diebold, U. *Phys. Rev. B: Condens. Matter Mater. Phys.* **2014**, *90*, 165438.
(37) Çelebi, C.; Ari, O.; Senger, R. T. *Phys. Rev. B: Condens. Matter Mater. Phys.* **2013**, *87*, 085308.
(38) Kresse, G.; Furthmüller, J. *Comput. Mater. Sci.* **1996**, *6*, 15.
(39) Kresse, G.; Furthmüller, J. *Phys. Rev. B: Condens. Matter Mater. Phys.* **1996**, *54*, 11169.
(40) Kresse, G.; Hafner, J. *Phys. Rev. B: Condens. Matter Mater. Phys.* **1993**, *47*, 558.
(41) Kresse, G.; Hafner, J. *Phys. Rev. B: Condens. Matter Mater. Phys.* **1994**, *49*, 14251.
(42) Klimeš, J.; Bowler, D. R.; Michaelides, A. *Phys. Rev. B: Condens. Matter Mater. Phys.* **2011**, *83*, 195131.
(43) Dion, M.; Rydberg, H.; Schröder, E.; Langreth, D. C.; Lundqvist, B. I. *Phys. Rev. Lett.* **2004**, *92*, 246401.
(44) Hofer, W. A.; Foster, A. S.; Shluger, A. L. *Rev. Mod. Phys.* **2003**, *75*, 1287.
(45) Tersoff, J. *Phys. Rev. B: Condens. Matter Mater. Phys.* **1989**, *40*, 11990.
(46) Tersoff, J. *Phys. Rev. B: Condens. Matter Mater. Phys.* **1990**, *41*, 1235.

DOI: 10.1021/jacs.5b08227
J. Am. Chem. Soc. 2015, 137, 16049−16054